Optimization of Permanently Polarized Hydroxyapatite Catalyst. Implications for the Electrophotosynthesis of Amino Acids by Nitrogen and Carbon Fixation

Jordi Sans,[1] Vanesa Sanz,[2] Luis J. del Valle,[1] Jordi Puiggalí,[1,3] Pau Turon,[2,] and Carlos Alemán[1,3,*]*

[1] Departament d'Enginyeria Química and Barcelona Research Center for Multiscale Science and Engineering EEBE, Universitat Politècnica de Catalunya, C/ Eduard Maristany 16, Barcelona 08019, Spain.

[2] B. Braun Surgical, S.A.U. Carretera de Terrassa 121, 08191 Rubí (Barcelona), Spain

[3] Institute for Bioengineering of Catalonia (IBEC), The Barcelona Institute of Science and Technology, Baldiri Reixac 10-12, 08028 Barcelona Spain

[*] Correspondence to: pau.turon@bbraun.com and carlos.aleman@upc.edu

Abstract

The enhanced catalytic activity of permanently polarized hydroxyapatite, which is achieved using a thermally stimulated polarization process, largely depends on both the experimental conditions used to prepare crystalline hydroxyapatite from its calcium and phosphate precursors and the polarization process parameters. A mineral to brushite, which is an apatitic phase that can evolve to hydroxyapatite, is found at the surface of highly crystalline hydroxyapatite. It appears after chemical precipitation and hydrothermal treatment performed at 150 ºC for 24 h followed by a sinterization at 1000 ºC and a polarization treatment by applying a voltage of 500 V at high temperature. Both the high crystallinity and the presence of brushite-like phase on the electrophotocatalyst affect the nitrogen and carbon fixation under mild reaction conditions (95 ºC and 6 bar) and the synthesis of glycine and alanine from a simple gas mixture containing N_2, CO_2, CH_4 and H_2O. Thus, the Gly/Ala ratio can be customized by controlling the presence of brushite on the surface of the catalyst, enabling to develop new strategies to regulate the production of amino acids by nitrogen and carbon fixation.

Keywords: Brushite; Catalytic apatites; Carbon dioxide fixation; Heterogeneous catalysis; Hydrothermal synthesis; Molecular nitrogen fixation; Thermally stimulated polarization

1. Introduction

Synthetic mineral hydroxyapatite (HAp), a crystalline form of calcium phosphate with formula $Ca_{10}(PO_4)_6(OH)_2$, is of major biomedical interest because of its compositional and structural similarity with bones and teeth, which has motivated its use to repair and reconstruct such hard tissues [1-5]. HAp has a hexagonal structure with space group $P6_3/m$ and cell dimensions $a=b=$ 9.42 Å and $c=$ 6.87 Å, which is stable up to 1273 ºC [6]. However, the properties of this structure can be tuned by introducing a large number of anionic and cationic substituents, enabling the utilization of HAp for other applications. Among those, the catalytic activity of HAp has been the subject of numerous publications and patents [7-15].

The electrical properties of HAp were found to be of interest for its biomedical application. Thus, there was an early research dealing with the polarization of HAp by applying a DC electric potential (*i.e.* from 1.0 to 10.0 kV/cm) at elevated temperatures (*i.e.* from 200 ºC to 800 ºC) to generate a surface charge [16-22]. Such process causes defects inside crystal grains and originates space charge polarization in the grain boundaries, both inducing the formation of electrical dipoles. However, the relaxation of such dipoles through time suggested that polarization was only partially maintained (*semi-permanent*), even though this effect was not quantified. The presence of HAp surface charge affects the growth of apatite bone [16-20], which is accelerated and decelerated on negative and positive charged surfaces, respectively, and promotes adhesion of osteoblastic cells [21, 22], which has been attributed to the improved wettability of polarized HAp.

In order to enhance the activity of already existing catalysts or to create new catalysts, two different approaches [23, 24] have been developed to synthesize *permanently* polarized HAp. The first one was based on the electrochemical synthesis of

a thin HAp coating from an aqueous solution onto a stainless steel or titanium electrode using a voltage of 3-4 V to induce the electrolysis of water, which resulted in giant electrical polarization normal to the surface of the coating [23]. Yttrium- and fluorine co-doped HAp coatings synthesized using this methodology were recently used as TiO_2 photocatalyst support [25], which was used to catalyze the photochemical reduction of aqueous silver ions to produce silver nanoparticles. It was found that photo-generated electrons and holes in the catalysts were driven in different directions by the polarization co-doped HAp support, improving the photocatalytic activity of TiO_2.

In the second approach, we prepared permanently polarized mineral by applying a constant DC voltage of 500 V (*i.e.* DC field of 3 kV/cm) at 1000 ºC for 1 h to previously sintered crystalline HAp (cHAp) [24]. This process, hereafter denoted *Thermally Stimulated Polarization* (TSP) process, caused important chemical changes, as the formation of OH^- defects (vacancies) and structural variations that resulted in an increment of the crystallinity. Consequently, the electrochemical properties and electrical conductivity of the resulting polarized mineral, hereafter denoted cHAp/tsp, increased noticeably when compared with cHAp. Moreover, the ability to adsorb inorganic phosphates and phosphonates was around 1.5-2 times higher for cHAp/tsp than for the non-polarized mineral [24, 26], which is very important for the fabrication of scaffolds for bone regeneration. Besides, an electrophotocatalyst based on cHAp/tsp discs coated with zirconyl chloride (ZC) and aminotris(methylenephosphonic acid) (ATMP) was used to fix nitrogen from N_2 and carbon from CO_2 and CH_4 obtaining both glycine (Gly) and alanine (Ala; D/L racemic mixture) amino acids under mild reaction conditions (*i.e.* from 1 to 6 bars and 95 ºC) by [27, 28].

In this work we examine the influence of different experimental parameters on the properties of cHAp and cHAp/tsp. Specifically, we have studied the influence of: *i*)

temperature and the duration of the hydrothermal treatment (HT) used to prepare HAp before to transform it into cHAp through the sintering process; and *ii*) the strength of the electric field and the geometry of the electrodes applied to cHAp during the TSP process. The structure of the resulting cHAp and cHAp/tsp minerals has been analyzed by Raman spectroscopy, scanning electron microscopy (SEM) and wide angle X-ray diffraction (WAXD). After this, the influence of the structural changes induced by some of such experimental parameters on the electrophotocatalytic fixation of N_2, CO_2 and CH_4 has been examined. For this purpose, different catalysts were prepared by incorporating ZC and ATMP to cHAp/tsp and the products of reactions conducted at 95 ºC and 6 bar have been analyzed by nuclear magnetic resonance (NMR) spectroscopy. The reaction yield has been found to be intimately connected with the cHAp/tsp structure of the electrophotocatalysts.

2. Methods

2.1. Materials

Calcium nitrate $Ca(NO_3)_2$, diammomium hydrogen phosphate [$(NH_4)_2HPO_4$; purity > 99.0%], ammonium hydroxide solution 30% [NH_4OH; purity: 28-30% w/w], zirconyl chloride (ZC; $ZrOCl_2 \cdot 8H_2O$) and aminotris(methylene phosphonic acid) (ATMP) were purchased from Sigma Aldrich. Ethanol (purity > 99.5%) was purchased from Scharlab. All experiments were performed with milli–Q water. N_2, CH_4 and CO_2 gases with a purity of >99.995% were purchased from Messer.

2.2. Synthesis of crystalline hydroxyapatite (cHAp)

15 mL of 500 mM $(NH_4)_2HPO_4$ in de-ionized water (pH adjusted to 10.5 ± 0.2 with ammonium hydroxide) were added drop-wise (2 mL/min) and gentle agitation (100

rpm) to 25 mL of 500 mM $Ca(NO_3)_2$ in ethanol. This represents an important change with respect to previous works [27,28], in which the pH was increased by adding ammonium hydroxide to the $Ca(NO_3)_2$ ethanol solution. The mixture was stirred for 1 h (100 rpm) at room temperature. HT was applied to the suspension with temperature (T_h) ranging from 50 ºC to 240 ºC using an autoclave Digestec DAB-2 for 24 h unless otherwise is specified. The autoclave is allowed to cool down before opening. The white precipitates were separated by centrifugation and washed sequentially at 8000 rpm for 5 minutes with water and a 60/40 v/v ethanol/water mixture (twice). After freeze–drying for 3 days the powder obtained was sintered at 1000 ºC during 2 h at an air atmosphere. Hereafter, samples obtained using this procedure have been denoted cHAp(T_h), where T_h refers to the temperature used for the HT of HAp.

2.3. Thermally stimulated polarization process (TSP)

150 mg of sintered cHAp powder were uniaxially pressed at 620 MPa for 10 minutes (*i.e.* 5 tons of applied weight) to obtain a disc of 10 mm of diameter and 1 mm of thickness. The disc was placed in between two stainless steel (AISI 304) plates separated at 4 cm and heated at 1000 ºC in air atmosphere. Then, a DC voltage of 100, 500 or 1000 V was applied during 1 h. Hereafter, samples obtained by applying the TSP process to cHAp(T_h) are denoted cHAp/tsp(T_h), the applied voltage being explicitly indicated in each case.

2.4. Characterization of the cHAp(T_h) and cHAp/tsp(T_h)

The structural fingerprint of the samples was studied using the inVia Qontor confocal Raman microscope (Renishaw), equipped with a Renishaw Centrus 2957T2 detector. All measurements were performed with a 785 nm laser. In order to achieve

representative results, all the spectra presented in this study are the result of the average of a 105×90 μm grid with 42 points. Depth profiles were also obtained using the same equipment.

Morphological characterization was performed by scanning electron microscopy (SEM) using a Focused Ion Beam Zeiss Neon40 microscope equipped with a SEM GEMINI column with a Shottky field emission. Samples were sputter-coated with a thin layer of carbon to prevent sample charging problems.

Crystallinity (χ_c) was obtained by wide angle X-ray scattering (WAXS) using a Brucker D8 Advance model with Bragg-Brentano 2θ configuration and Cu K_α radiation (λ = 0.1542 nm). A one-dimensional Lynx Eye detector was employed. Measurements were performed in a 2θ range of 20º - 60º in steps of 0.02º, and scan speed of 2 s. The χ_c value was obtained using the following expression:

$$\chi_c = 1 - \frac{V_{112/300}}{I_{300}} \qquad (1)$$

where I_{300} is the intensity of the (300) reflection and $V_{112/300}$ is the intensity of the hollow between the (112) and (300) reflections. The crystallite size, L_{hkl}, was calculated using the Debye-Scherrer equation

$$L_{hkl} = \frac{0.9 \cdot \lambda}{B \cdot \cos\theta_{hkl}} \qquad (2)$$

where λ is the wavelength of the monochromatic X-ray beam, B is the full width at half maximum of the peak at the maximum intensity, and θ_{hkl} is the peak diffraction angle that satisfies the Bragg's law for the (hkl) plane.

2.5. Preparation of the cHAp/tsp-based catalyst

The 3-component catalyst was prepared by dropping successively 100 μL of 50 mM ATMP, 10 mM ZC and 50 mM ATMP aqueous solutions on a cHAp/tsp disk (diameter:

10 mm; thickness: 1 mm). Before each dropping step, the sample was kept 8 h at room temperature for drying.

2.6. Synthesis of amino acids

A high pressure stainless steel reactor was employed to perform the synthesis of amino acids [27]. The reactor was also characterized by an inert reaction chamber (120 mL) coated with a perfluorinated polymer where both catalyst and water were incorporated. The reactor was equipped with an inlet valve for the entrance of N_2, CH_4, CO_2 and an outlet valve to recover the gaseous reaction products. A UV lamp (GPH265T5L/4, 253.7 nm) was also placed in the middle of the reactor to irradiate the catalyst directly, the lamp being protected by an UV transparent quartz tube. All surfaces were coated with a thin film of a perfluorinated polymer in order to avoid any contact between the reaction medium and the reactor surfaces, in this way discarding other catalytic effects.

In this work the reactions were performed at 95 ºC for a reaction time of 48 or 72 h. Catalyst samples weighed approximately 150 mg and 0.5 mL of de-ionized liquid water were initially incorporated into the reaction chamber. The chamber was extensively purged with the first selected gas in order to eliminate the initial air content. Each selected gas was introduced to increase the reaction chamber pressure (measured at room temperature) to the target pressure. In all cases the chamber pressure was increased up to 6 bar by introducing sequentially 2 bar of each feeding reaction gas.

The reaction products were analyzed by NMR spectroscopy. ^{1}H NMR spectra were acquired with a Bruker Avance III-400 spectrometer operating at frequencies of 400.1 MHz for ^{1}H and ^{13}C NMR spectra were obtained using a Bruker DRX-500-Cryo operating at 500.1 MHz. Chemical shifts were calibrated using tetramethylsilane (^{1}H

and ^{13}C) as internal standard. 64 and one 4800 scans were recorded for ^{1}H and ^{13}C NMR, respectively. In order to remove the amino acids from the catalyst, samples were dissolved in deuterated water containing 100 mM of HCl and 50 mM of NaCl with the final addition of deuterated water.

3. Results and discussion

3.1. cHAp: Temperature for the hydrothermal treatment

As mentioned above, in this work cHAp refers to the sintered mineral once HAp has been precipitated and hydrothermally treated. The preparation of cHAp with the right stoichiometry, high aspect ratio and high crystallinity remains difficult to obtain. The precipitation and HT of HAp are crucial steps to adjust the stoichiometry and avoid the formation of other phases, such as β-tricalcium phosphate (βTCP) that can be easily formed depending on the conditions, and the sintering at 1000-1200 ºC is frequently used to refine the crystal structure [29].

Figure 1a compares the Raman spectra recorded for cHAp(T_h) samples prepared by applying, after the precipitation step, a HT at T_h= 50, 100, 150, 200 and 240 ºC for 24 h. The values of the normal-mode frequencies of the PO_4^{3-} tetrahedron typically observed from Raman measurements in aqueous solution are υ_1= 938 cm^{-1}, υ_2= 420 cm^{-1}, υ_3= 1017 cm^{-1} and υ_4= 567 cm^{-1} [30]. In cHAp and βTCP, the crystalline field causes not only the shifts but also the splitting of the PO_4^{3-} normal modes, even though these effects depend on the crystallographic structure. The spectra displayed in Figure 1a clearly indicates that the splitting of the PO_4^{3-} normal modes decreases with increasing T_h. For example, a single intense peak arising from the non-degenerate υ_1 mode of PO_4^{3-} at 962 cm^{-1} is detected in the spectra of cHAp($T_h \geq 100$ ºC) samples, whereas several peaks can be observed for cHAp(50 ºC). A similar feature is observed for the

doubly degenerate υ_2 and triply degenerate υ_3 and υ_4, which span a frequency range of 400-490, 570-625 and 1020-1095, respectively, for cHAp($T_h \geq 100$ ºC). In all cases the PO_4^{3-} bands appear at frequencies 20-25 cm^{-1} higher than those corresponding to the free-tetrahedral normal modes (*i.e.* in aqueous solution).

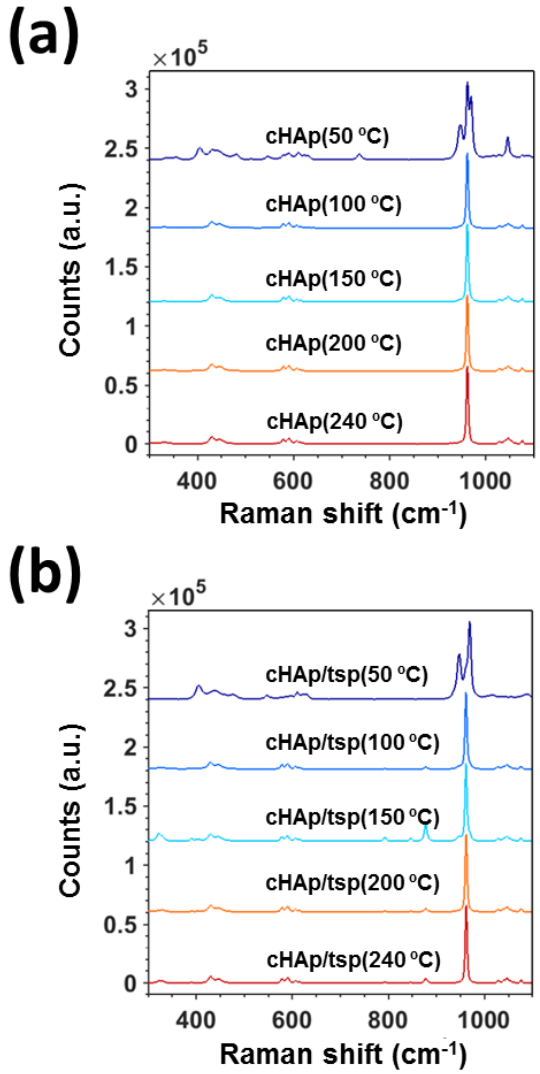

Figure 1. Raman spectra of (a) cHAp(T_h) and (b) cHAp/tsp(T_h) prepared using different hydrothermal temperatures for 24 h.

cHAp exhibits a $P6_3/m$ space group and the unit cell contains six equivalent PO_4^{3-} tetrahedrons [31], whereas βTCP crystallizes in the R3c space group and its unit cell contains 42 PO_4^{3-} tetrahedrons distributed in three non-equivalent types [32].

Consequently, the single intense peak detected at υ_1= 962 cm^{-1} is observed as a two peaks and a shoulder for βTCP [33]. This structural difference also affects υ_2 and υ_4, which span over a higher frequency range in βTCP than in cHAp. Moreover, υ_2 and υ_4 are separated by a frequency gap of only 55 cm^{-1} in βTCP, while the gap is of 120 cm^{-1} in cHAp. As it can be seen in Figure 1a, the fingerprints of the spectrum recorded for the cHAp(50 ºC) sample agree with those expected for βTCP, indicating that this is the predominant phase when the HT is performed at low temperature.

The normal modes of PO_4^{3-} in the Raman spectra obtained for cHAp/tsp(T_h), which are displayed in Figure 1b, show similar features to those described for cHAp(T_h) (Figure 1a). After the TSP treatment, the intensity and width of the peaks associated to the PO_4^{3-} correspond to the βTCP phase for the samples prepared at T_h= 50 ºC, while cHAp is clearly identified in samples hydrothermally treated at $T_h \geq$ 100 ºC. However, some distinctive features can be also identified in cHAp/tsp(T_h) samples as a function of T_h. For example, cHAp/tsp(150 ºC) shows weak peaks at around 330 cm^{-1} (see below for discussion), whereas no signal is detected for the rest of the samples. Considering that the detection of these peaks depends on the degree of crystallinity of the sample, Raman results suggest that the highest crystallinity is achieved when the HT is performed at T_h= 150 ºC. Furthermore, a peak at 878 cm^{-1} is detected for cHAp/tsp($T_h \geq$ 100 ºC), as is clearly in the evidenced in Figure 2a. This signal, which is characteristic of the Brushite mineral (*i.e.* $CaHPO_4 \cdot 2H_2O$) that is understood to be a precursor of apatite [34], has been attributed to the normal mode frequency of HPO_4^{2-} [33, 34]. The intensity of this band is much greater for the sample obtained at T_h= 150 ºC, while for the rest it is observed as a weak peak. In addition, two bands typical of POH rotation and deformation modes appear at 794 and 848 cm^{-1} [36, 37]. Although they are very

weak in all cases, POH signals also showed the highest intensity for samples obtained at T_h= 150 ºC.

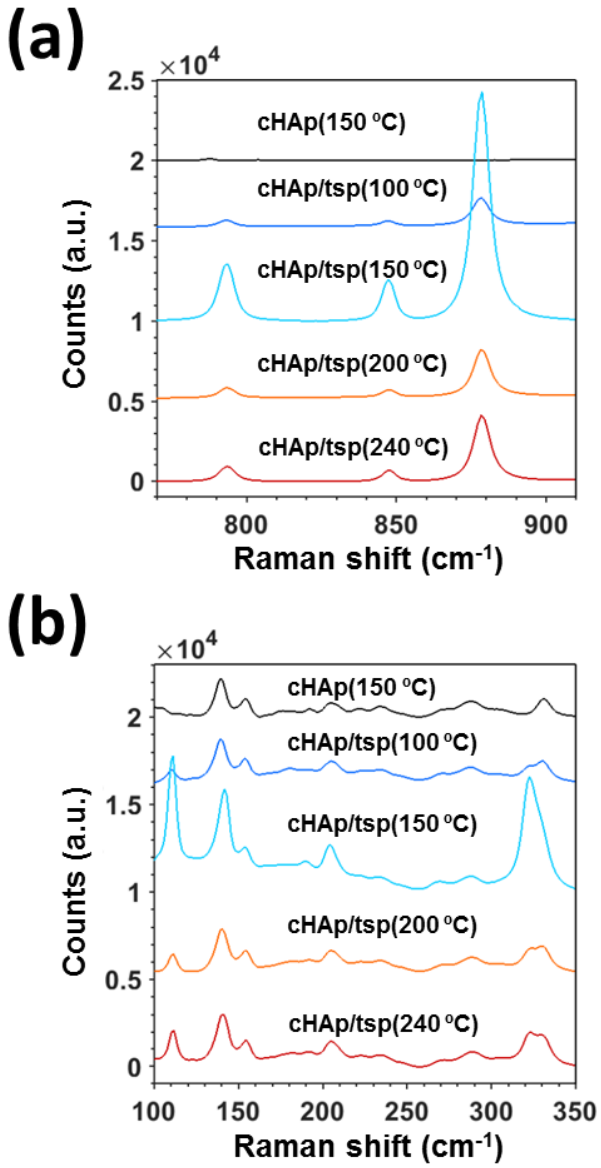

Figure 2. Raman spectra in the (a) 770-910 cm^{-1} and (b) 100-350 cm^{-1} intervals of cHAp(150 ºC) and cHAp/tsp($T_h \geq$ 100 ºC).

Figure 2b compares the weak intensity bands observed between 100 and 350 cm^{-1} for cHAp(150 ºC) and cHAp/tsp($T_h \geq$ 100 ºC). These bands have been attributed to translational modes of the Ca^{2+} (111, 139 and 154 cm^{-1}), PO_4^{3-} (287 cm^{-1}) and OH^- (331 and 323 cm^{-1}) sub-lattices, and rotational modes of the PO_4^{3-} group (205 cm^{-1}) [33, 38,

39]. As it can be seen, both the intensity and narrowness of all these bands is maximal when the TSP process is applied to cHAp(150 ºC) samples. Moreover, the intensity of bands associated to the translational modes of the OH^- sub-lattice yield (331 and 323 cm^{-1} in Figure 2b) increases linearly with that of the POH rotation and deformation modes (794 and 848 cm^{-1} in Figure 2a), evidencing a structural correlation.

3.2. Duration of the HT and characteristics of the TSP treatment

The duration of the HT is another factor that significantly affects the structure of the HAp and, therefore, the performance of cHAp/tsp as catalyst. Figure 3a compares the Raman spectra recorded for samples prepared at T_h= 150 ºC when the time for the HT was of 10 or 24 h. As it can be seen, the spectra of the cHAp samples obtained after a HT of only 10 h show the peaks described in the previous section for the βTCP phase. Thus, the re-ordering of the βTCP phase into cHAp is only completed when the HT is long enough, even when the T_h was the optimal. Although similar conclusions were reported in previous studies [40, 41], which indicated that 24 h is the optimum time for the HT, the influence of the TSP process on samples obtained using shorter hydrothermal times was never studied before. Interestingly, Figure 3a shows that the TSP treatment favors the re-arrangement of the surface in samples prepared using both 10 and 24 h, as is proved by the apparition of the Brushite-like peak at 878 cm^{-1} and the translational modes of the OH^- sub-lattice at 323 cm^{-1}. Nevertheless, the βTCP fingerprints identified for cHAp(150 ºC) samples obtained using a treatment time of 10 h, which are associated to the four normal-mode frequencies of the PO_4^{3-}, remain practically unaltered after the permanent polarization process. Accordingly, the TSP process cannot be used to compensate the undesirable structural effects induced by the shortening of the HT.

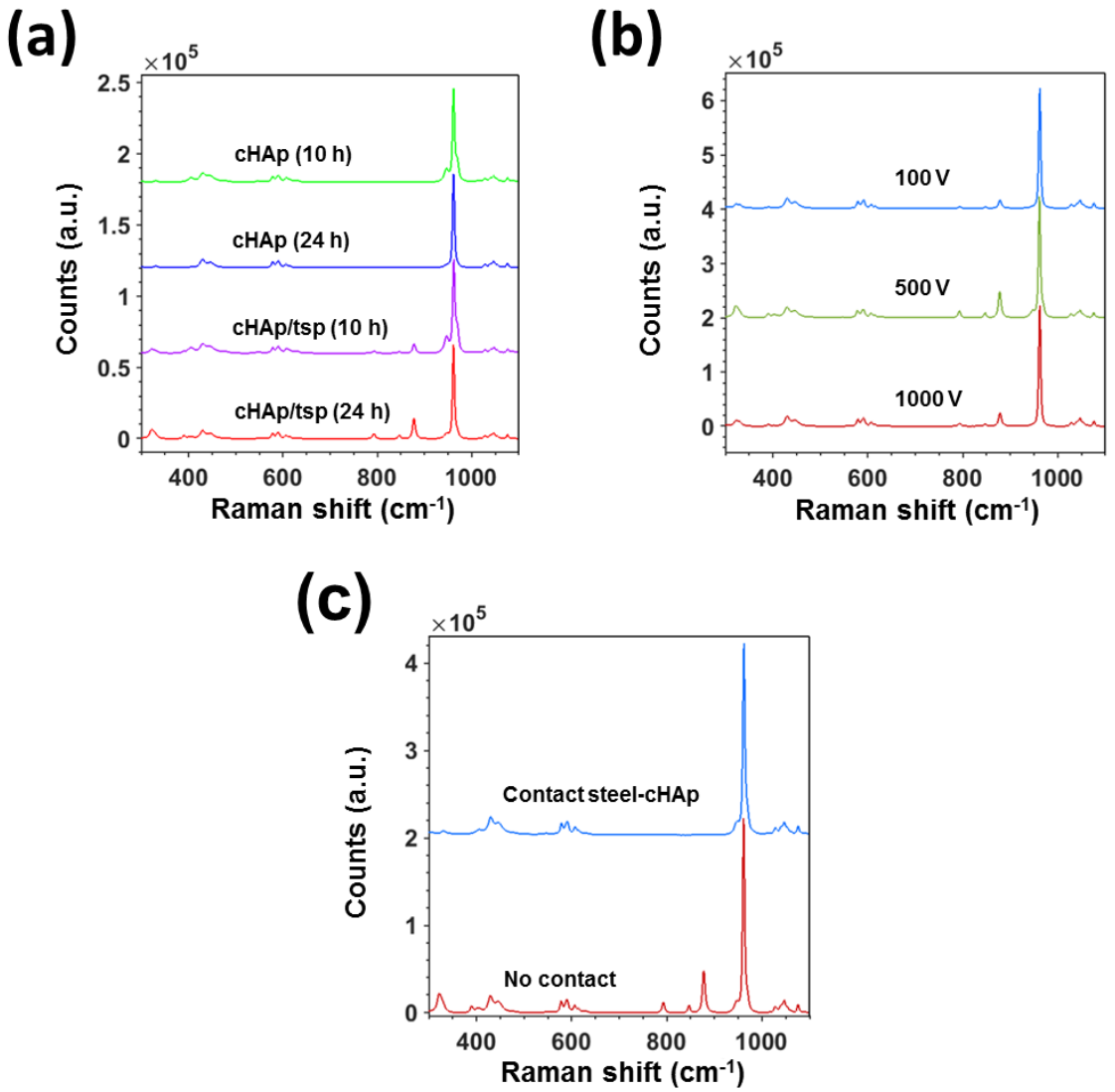

Figure 3. (a) Raman spectra of cHAp(150 ºC) and cHAp/tsp(150 ºC) prepared using different times for the HT: 10 h and 24 h. (b) Raman spectra of cHAp/tsp(150 ºC) prepared by applying different DC voltages to cHAp(150 ºC). (c) Raman spectra of cHAp/tsp(150 ºC) prepared by applying a voltage of 500 V and maintaining the steel electrodes in contact or not with the cHAp(150 ºC) samples. cHAp(150 ºC) were prepared applying the HT for 24 h in both (b) and (c).

The effect of the electric field strength used to induce permanent polarization in cHAp has been examined by applying DC voltages of 100, 500 or 1000 V (25, 125, 250 $V \cdot cm^{-1}$ respectively) to cHAp(150 ºC) samples. Although the Raman spectra obtained for all the resulting samples correspond to cHAp (Figure 3b), some bands apparently associated to the catalytic activity of cHAp/tsp are slightly influenced by the strength of

the DC voltage. More specifically, the peaks attributed to translation modes of the OH^- sub-lattice (323 cm^{-1}), the normal mode of HPO_4^{2-} (878 cm^{-1}), and the POH rotation and deformation modes (794 and 848 cm^{-1}) are more intense and better defined for samples polarized at 500 V than for those obtained at 100 and 1000 V. According to these results, the alteration of the voltage used for the TSP process is not expected to annihilate the activity of cHAp/tsp as catalyst but to induce small changes in its effectivity.

Finally, the influence of the geometry of the electrodes in the TSP treatment was investigated. For such purpose, cHAp/tsp(150 ºC) samples were prepared using a DC voltage of 500 V and two different geometries for the electrodes: *i)* steel plates separated at 4 cm and, therefore, the cHAp(150 ºC) disc was in contact with one electrode only (*i.e.* the thickness of the sintered mineral discs was 1 mm); and *ii)* steel plates separated at 1 mm and, therefore, each side of the cHAp(150 ºC) disc was in contact with an electrode. The recorded Raman spectra, which are compared in Figure 3c, reveal that the bands at 794, 848 and 878 cm^{-1} are only observed when the TSP process is conducted hindering the steel-cHAp contact. Also, the intensity of the band associated to the translational mode of the OH^- sub-lattice (323 cm^{-1}) is much higher when the separation between the electrodes is of 4 cm. This variation has been attributed to the OH^- exchange with the atmosphere [42].

A depth profiling Raman analysis was conducted to monitor the extent of the changes induced by the TSP treatment. Figure 4a compares the Raman spectra recorded at different depths (*i.e.* from the surface to a depth of 95 μm) for cHAp/tsp(150 ºC) prepared applying the HT for 24 h and using a polarizing voltage of 500 V at 1000 ºC. Although the spectra show the same fingerprints in all cases, the intensity of the signals decreases with increasing depth. This is observation is particularly remarkable for the

bands of HPO_4^{2-} (878 cm^{-1}) and both POH rotation and deformation modes (794 and 848 cm^{-1}). These results allow us to conclude that the changes caused by the TSP treatment are predominantly located at the surface of the mineral. This is corroborated in Figure 4b, which displays the intrinsically weak bands detected in the 110 and 330 cm^{-1} region. The intensity of the bands associated to the rotational modes of the PO_4^{3-} group (205 cm^{-1}) and, specially, to the translational modes of the Ca^{2+} (111, 139 and 154) cm^{-1}), PO_4^{3-} (287 cm^{-1}) and OH^- (323 cm^{-1}) sub-lattices decreases with increasing depth.

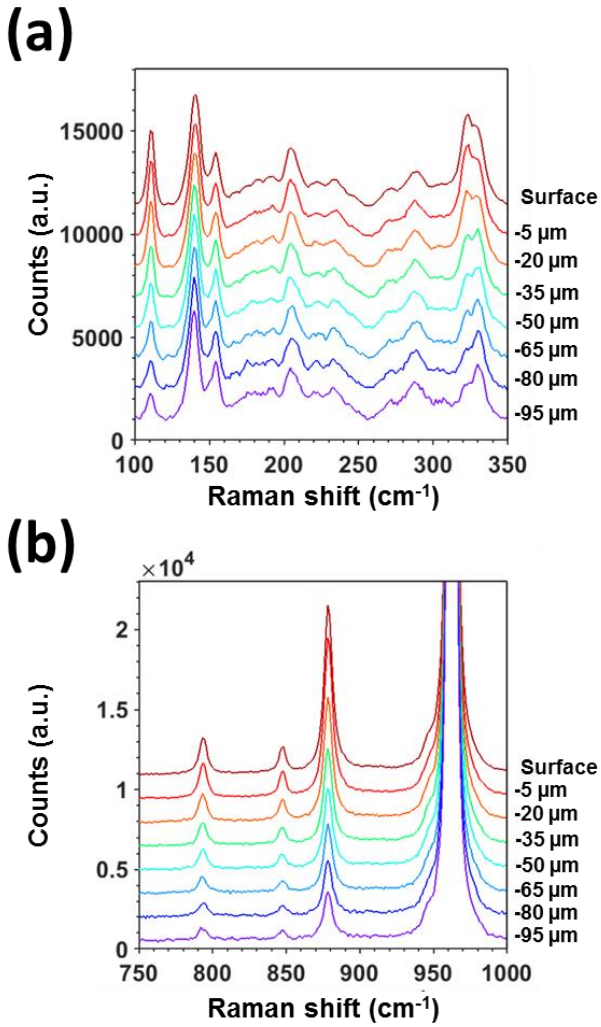

Figure 4. (a) Raman spectra at different depths of cHAp/tsp(150 ºC) obtained applying the HT for 24 h and a polarizing voltage of 500 V at 1000 ºC. (b) Magnification of the spectra displayed in (a) for the 100-350 cm^{-1} region.

3.3. Morphological and structural characterization of cHAp samples

Raman spectra displayed in Figures 1 and 2 indicate that the chemical properties of cHAp(T_h) and cHAp/tsp(T_h) depend on T_h and, therefore, the catalytic activity of the latter, as will be shown in next sections. In this section, we use SEM and XRD to investigate the implications of T_h in the morphology and structure of cHAp.

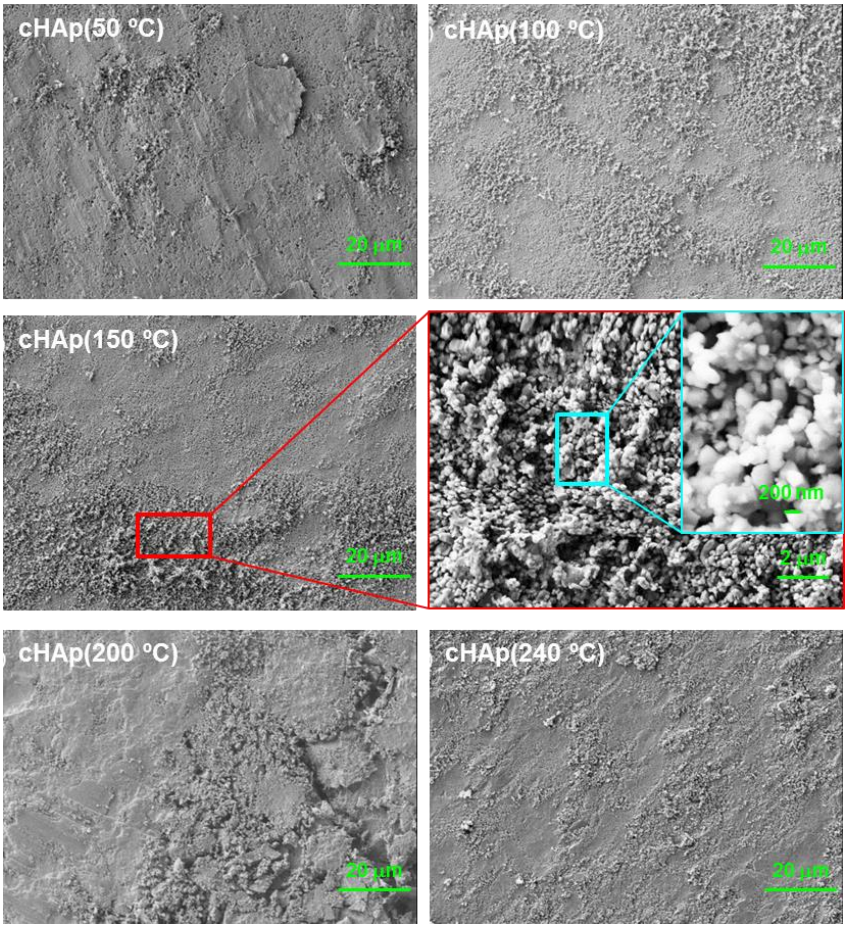

Figure 5. Low magnification SEM micrographs of cHAp(T_h) with T_h= 50, 100, 150, 200 and 240 ºC. In all cases the HT was applied for 24 h. High magnification micrographs of cHAp(150 ºC) are also displayed.

Low magnification SEM micrographs of cHAp(T_h) with T_h= 50, 100, 150, 200 and 240 ºC are displayed in Figure 5. With the exception of the sample with βTCP (T_h= 50 ºC), which presents the most compact surface, the rest of the samples present a morphology made of compact regions alternated with extensive porous zones.

Inspection of the high magnification micrographs, shown in Figure 5 for cHAp(150 ºC) as representative sample, indicate that porous zones are constituted by pillars that grow through the aggregation of mineral nanoparticles in a preferential direction. However, the morphology of the porous areas is apparently independent of T_h, as is evidenced in Figures S1 and S2 that shows high magnification micrographs of cHAp prepared using T_h= 100 and 240 ºC, respectively. Therefore, the morphology cannot be properly used as a distinctive feature for the identification of cHAp(T_h) samples with appropriated characteristics for the manufacture of catalysts with maximal catalytic activity.

Structural characterization of prepared cHAp(T_h) samples was completed by WAXD (Figure 6a). The characteristic fingerprint of hexagonal crystal symmetry cHAp (a= b= 9.421 Å, c= 6.881 Å, α= β= 90º, and γ= 120º; JCPDS card number 9-0432) [43] is typically associated to the peaks at 32º-34º 2θ, which correspond to the (211), (112) and (300) reflections. Those reflections are clearly identified in the diffraction profiles of all samples prepared using $T_h \geq$ 100 ºC and can only be intuited in cHAp(50 ºC) sample. Other characteristic reflection peaks of cHAp appear at 2θ= 32º, 34º, 40º, 47º and 49º, which correspond to (211), (202) (130) (222) and (214) reflections. The (112) and (300) peaks were also used to determine the crystallinity (χ_c: Eqn 1), whereas the (211) reflection was used to calculate the crystallite size (L_{211}; Eqn 2). The χ_c of cHAp(T_h) is 0.53, 0.82, 0.68 and 0.77 for T_h= 100, 150, 200 and 240 ºC, respectively, which is fully consistent with Raman spectra displayed in Figure 1a. Thus, the χ_c of cHAp is maximal when it is prepared at T_h= 150 ºC followed by the one obtained at T_h= 240 ºC. The variation detected in cHAp(200 ºC) with a decrease in χ_c in relation to cHAp(150 ºC) and cHAp(240 ºC), and which is experimentally reproducible, has been attributed to a combined effect of the lyophilization and sintering processes on the crystals, which seems to depend on the value of T_h used. This could not only explain the reduction of χ_c

when T_h increases from 150 ºC to 200 ºC but also the fact that χ_c is lower for cHAp(240 ºC) than for cHAp(150 ºC). Besides, the calculated L_{211} values correspond to 69.1, 82.7, 82.6 and 82.7 nm for cHAp(T_h) with T_h= 100, 150, 200 and 240 ºC, respectively.

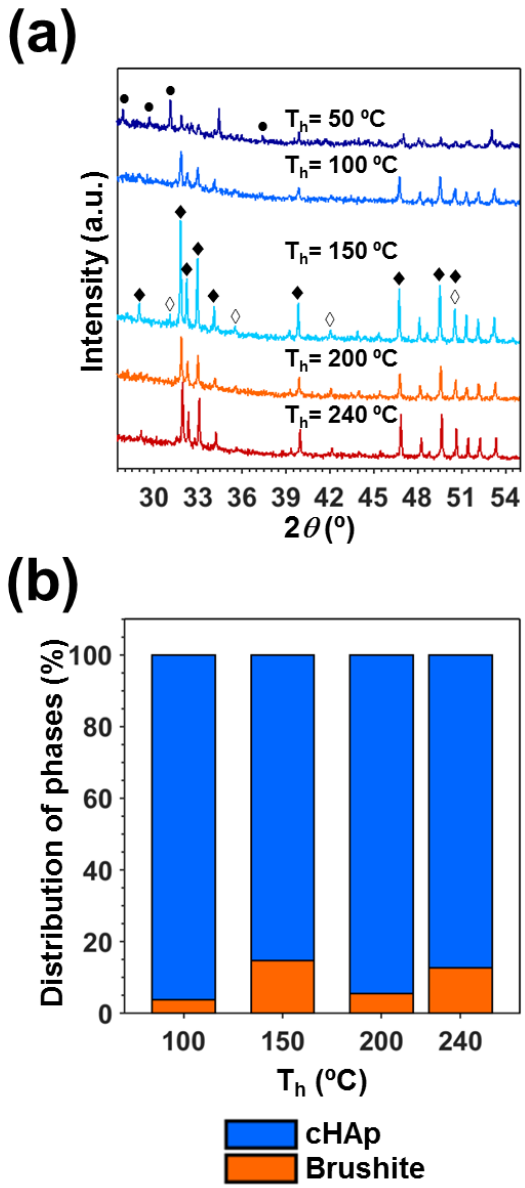

Figure 6. (a) X-ray diffraction patterns corresponding to cHAp(T_h) with T_h= 50, 100, 150, 200 and 240 ºC. In all cases the HT was applied for 24 h. Reflections attributed to cHAp and brushite are marked by filled diamonds and empty diamonds, respectively, in the diffractogram of cHAp(150 ºC), while those associated with βTCP are indicated by filled circles in the diffractogram of cHAp(50 ºC). (b) Distribution of cHAp and brushite phases in cHAp(T_h) with $T_h \geq$ 100 ºC. This was obtained from the (211) reflection of cHAp and the (141) reflection of brushite.

On the other hand, the most relevant reflection peaks of brushite (JCPDS card number 72-0713) [44], which has a monoclinic structure with cell parameters *a*= 5.812 Å, *b*= 15.180 Å, *c*= 6.239 Å, α=γ= 90º and β= 116.43º, are clearly observed in the X-ray diffraction pattern of cHAp(150 ºC) (Figure 6a). These reflections, which are weaker for cHAp(240 ºC) and much weaker for cHAp(100 ºC) and cHAp(200 ºC), correspond to the (141), (121), $(15\bar{2})$ and $(14\bar{3})$ with 2θ= 29º, 35º, 42º and 51º, respectively. It is worth mentioning that, although the position of some of these reflections, as for example the $(14\bar{3})$, matches other reflections found in the theoretical diffraction of pure cHAp [45], the changes in the relative intensities points to co-existence of the two phases, which is in agreement with the Raman spectra. The amounts of cHAp and brushite-like phases in samples prepared at $T_h \geq 100$ were roughly estimated using X-ray diffraction patterns by comparing the (211) reflection of cHAp and the (141) reflection of brushite. Results show that, although the formation of the latter phase is promoted when the HT is conducted at $T_h \geq 100$ ºC (Figure 6b), cHAp is clearly the predominant phase in all cases. However, the content of the brushite-like phase increases from ~5% for T_h= 100 ºC and 200 ºC to ~15% for T_h= 150 ºC and 240 ºC.

In general the anomalous behavior of the samples obtained at T_h= 200 ºC has been attributed to the dehydration process reported for brushite at such temperature [46]. Thus, the layered structure of brushite, $CaHPO_4 \cdot 2H_2O$, in which mineral layers are held together by hydrogen bonded water molecules, converts into an amorphous phase and monetite, $CaHPO_4$ anhydrous. More specifically, although surface water evaporates at around 100 ºC, the two crystallographic water molecules of brushite, which are associated by hydrogen bonds with oxygen atoms in phosphate group, remain stable at

such temperature, leaving from the system at 200 ºC [46]. The structural transitions associated with brushite dehydration at 200 ºC explains the reduction of the χ_c, which in turn is in detriment of the catalytic activity, as is discussed in the next sub-section.

Finally, inspection of the diffractogram obtained for cHAp(50 ºC) (Figure 6a) allows to recognize the reflection peaks typically reported for βTCP (JCPDS card number 09016) [47], which predominate over those associated to the cHAp. Thus, the rhombohedral βTCP appears as the predominant crystalline phase in samples HT-treated at the lowest temperature.

3.4. Performance of cHAp/tsp(T_h) as catalyst for the synthesis of amino acids

In a recent study, we catalyzed the fixation of nitrogen from N_2 and carbon from CO_2 and CH_4 to obtain Gly and Ala, the two simplest amino acids [27, 28]. The catalyst was prepared by coating cHAp/tsp(150 ºC) samples with two layers of ATMP separated by an intermediate ZC layer. For this purpose, the cHAp/tsp(150 ºC) disks were sequentially immersed in 5 mM ATMP, 5 mM ZC and 1.25 mM ATMP aqueous solutions at room temperature for 5 h [27]. After each immersion, samples were dried at 37 ºC for 3 h. The catalyzed reaction was conducted under UV light irradiation and mild reaction conditions, in an inert reaction chamber starting from a simple gas mixture containing N_2, CO_2, CH_4 and H_2O.

In this work, the ATMP and ZC coatings were deposited onto the surface of cHAp/tsp(T_h) disks with T_h= 100, 150, 200 and 240 ºC, respectively. This deposition, which was done sequentially, was performed implementing important differences with respect to previous work [27]. Thus, the immersion process used to apply each coating layer was replaced by the sequential dropping of 100 μL of a 50 mM ATMP, 10 mM ZC and 50 mM ATMP aqueous solutions (Scheme 1). A drying interval period of 8 h

was left between each dropping step. Furthermore, the pH was regulated by adding ammonium hydroxide to the $(NH_4)_2HPO_4$ aqueous solution rather than to $Ca(NO_3)_2$ ethanol solution.

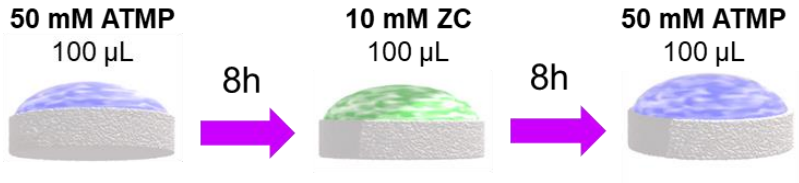

Scheme 1. Preparation of the cHAp/tsp(T_h)-based catalysts.

Figure 7 proves that changes in the application of the ATMP and ZC coatings does not alter the performance of the catalyst. Figure 7a shows the ^{1}H NMR spectrum of samples obtained by dissolving the catalyst prepared using cHAp/tsp(150 ºC) and the products of reaction after 48 h at 95 ºC. The signal corresponding to ATMP methylene group appears as doublet at 3.53-3.56 ppm, while the signals corresponding to the methylene group of produced Gly is a singlet at 3.37 ppm and both methine and methyl groups of Ala are the quadruplet at 3.84-3.87 ppm and the doublet at 1.60-1.62 ppm, respectively. The same compounds are also detected in the ^{13}C NMR spectrum displayed in Figure 7b), where only peaks assigned to the ATMP (53.82 and 52.92 ppm), Gly (172.26 and 41.35 ppm) and Ala (175.26, 50.56 and 16.18 ppm) units are detected. Figure S3 shows the ^{1}H NMR spectra obtained from control experiments using coated cHAp(150ºC) (*i.e.* without apply the TSP process) and from blank reactions (*i.e.* without catalyst), applying the same experimental conditions (48 h at 95 ºC). As it was expected, no product was obtained in such cases.

It should be noted that the reaction was positive for catalysts prepared using cHAp(T_h) with $T_h \geq 100$ºC but it was negative when the catalyst was obtained using the sample treated at $T_h = 50$ ºC. The yield of the reaction was calculated using commercial

Gly and Ala (purchased from Sigma-Aldrich) at a controlled concentration to calibrate the ^{1}H NMR peaks. The variation of the yield of the reaction expressed in % per cm^2 of catalyst against T_h is represented in Figure 8 for reactions of 48 h.

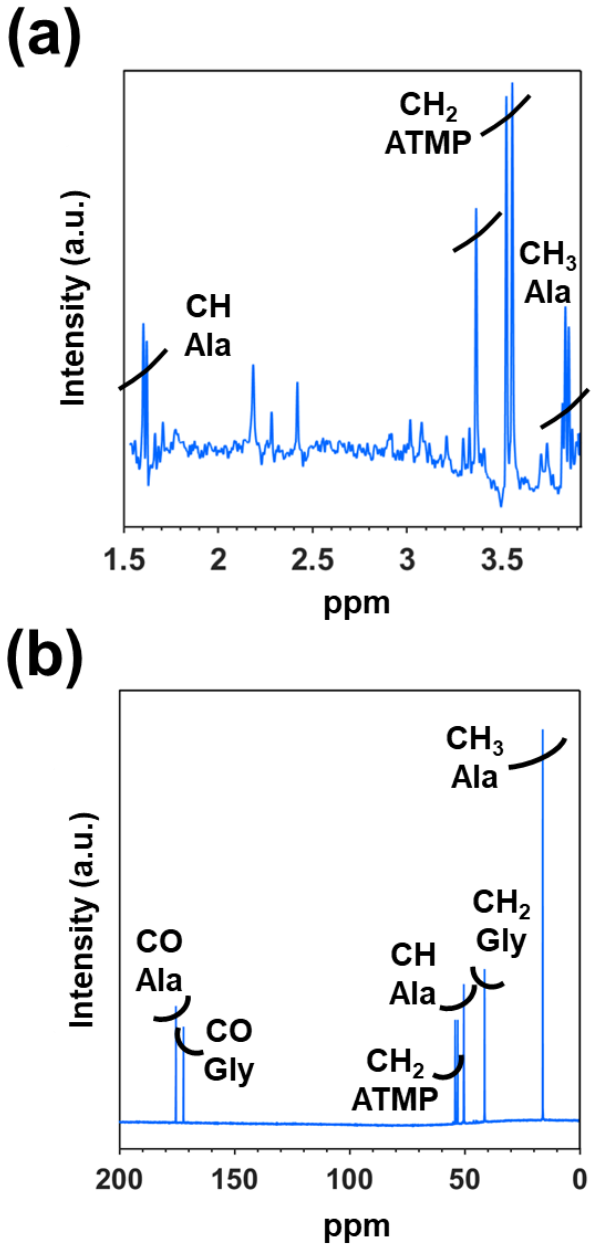

Figure 7. For sample obtained after reaction (95 ºC and 48 h) using a chamber pressure of 6 bar (*i.e.* 2 bar of each feeding reaction gas) and by the catalyst prepared using cHAp(150 ºC): (a) ^{1}H NMR and (b) ^{13}C NMR spectra of the solution obtained after extraction of the amino acids from the catalyst by dissolving the sample in deuterated water containing 100 mM of HCl and 50 mM of NaCl.

The yield of Ala was considerably higher than that of Gly in all cases. This was an expected result since the latter is the firstly formed compound in this catalytic process and should considering as a precursor of Ala, which is obtained by incorporating $\bullet CH_3$ radical coming from the decomposition of CH_4. However, the Gly/Ala ratio obtained using all successful catalysts is very high (Figure 8), varying from 4.1 (T_h= 100 ºC) to 3.6 (T_h= 150 ºC). These values are significantly higher than those found in our previous study, which was 2.5 after 48 h (*i.e.* Gly/Ala ratio decreased from 5.4 to 2.2 when the reaction time increased from 2 to 96 h) [27]. This feature has been attributed to the presence of the brushite phase, which was not observed in the catalyst prepared in our previous study. Accordingly, the combination of brushite and cHAp achieved with the process described in this work apparently accelerates the transformation of Gly into Ala.

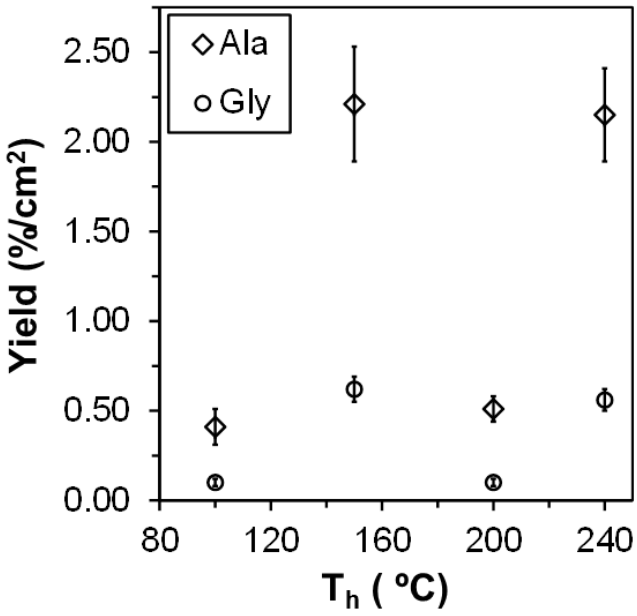

Figure 8. Yield (in % per cm^2 of catalyst) of Ala and Gly in the electrophotocatalytic fixation of N_2, CO_2 and CH_4 as a function of T_h. In all cases reactions (in triplicate) were performed at 6 bar and 95 ºC for 48 h.

The effect of the reaction on the yield is displayed in Table 1, which compares the results obtained using different catalysts (cHAp/tsp(T_h) with T_h = 50, 100 and 150 ºC)

and reaction times of 48 and 72 h. As it was expected, the yield of amino acids increases with the reaction time, the increment being of 80% and 62% for cHAp/tsp(100 ºC) and cHAp/tsp(150 ºC), respectively. Furthermore, the Gly/Ala ratio increased with the reaction time, reflecting the effect of the brushite phase in the kinetics of Gly-to-Ala conversion.

Table 1. Effect of the reaction time on the yield of Gly and Ala in the electrophotocatalytic fixation of N_2, CO_2 and CH_4 using cHAp/tsp(T_h). In all cases reactions (in triplicate) were performed at 6 bar and 95 ºC.

		Yield (%/cm^2)		
Catalyst	**Time**	**Gly**	**Ala**	**Gly/Ala**
cHAp/tsp(50 ºC)	48 h	-	-	-
	72 h	-	-	-
cHAp/tsp(100 ºC)	48 h	0.41 ± 0.10	0.10 ± 0.04	4.1
	72 h	0.77 ± 0.04	0.15 ± 0.02	5.1
cHAp/tsp(150 ºC)	48 h	2.21 ± 0.28	0.62 ± 0.08	3.6
	72 h	3.64 ± 0.24	0.95 ± 0.04	3.8

On the other hand, the yield correlates with both the χ_c and the brushite-like content in the cHAp/tsp(T_h). Thus, the maximum yield of amino acids after 48 h was obtained for the catalysts prepared at T_h= 150 ºC and 240 ºC (*i.e.* 2.8% and 2.7%, respectively), which displayed not only the highest χ_c (*i.e.* 0.82 and 0.77, respectively) but also the highest content of the brushite-like phase (*i.e.* 15% and 12%, respectively). In contrast, the total yield decreases one order of magnitude, ~0.5-0.6%, for reactions catalyzed by cHAp/tsp(T_h) samples with $\chi_c < 0.7$. This feature clearly reflects the very important role of the spatially translations modes, which facilitates the transport of charge at the surface through oscillation and translational molecular movements upon excitation of the lattice.

4. Conclusions

The experimental conditions used for the HT, after chemical precipitation of calcium phosphate, and the TSP treatment, after sintering, play a fundamental role in the structural properties of HAp and the activity of the resulting catalyst. cHAp samples prepared at T_h= 150 and 240 ºC exhibit the highest crystallinity, a significant amount of brushite-like phase (~15 %) and representative sub-lattice translational modes, which seems to play a crucial role in the electrophotocatalytic reaction to obtain Gly and Ala. Moreover, these structural characteristics are maintained, or even enhanced, when the TSP process is conducted applying a voltage of 500 V and avoiding the complete contact between the electrode and the mineral. Thus, results obtained from the catalytic fixation of N_2, CO_2 and CH_4 indicate that the highest yield of amino acids is obtained when the cHAp/tsp used as catalyst was prepared under such conditions. Moreover, a comparison with previous results, in which $CaHPO_4$ was eliminated from the surface of the catalyst, indicates that brushite accelerates the transformation of Gly into Ala. Accordingly, the Gly/Ala ratio obtained in this work is higher than in the previous work. Results imply that cHAp catalysts can be customized and used to develop new strategies to regulate the production of amino acids by nitrogen and carbon fixation. Within this context, more research about the role of cHAp coexisting with other phases different from brushite should be considered for the production of alternative catalysts.

Declaration of competing interest

Authors declare that the preparation and application of permanently polarized hydroxyapatite was patented by the Universitat Politcnica de Catalunya and B. Braun

Surgical S.A.U. (EP16382381, EP16382524, P27990EP00, PCT/EP2017/069437, EP20383003).

Acknowledgement

Authors acknowledge MINECO-FEDER (RTI2018-098951-B-I00 and RTI2018-101827-B-I00), Agència de Gestió d'Ajuts Universitaris i de Recerca (2017SGR359 and 2017SGR373) and B. Braun Surgical, S.A.U and B. Braun Melsungen AG for financial support. Support for the research of C.A. was received through the prize "ICREA Academia" for excellence in research funded by the Generalitat de Catalunya. Special thanks to Dr. Meinrad Lugan and Dr. Hans-Otto Maier for their support to the project.

Appendix A. Supplementary material

Supplementary data to this article can be found on line at https://doi.org./&&&.

References

[1] S. V. Dorozhkin, Biomaterials 31 (2010) 1465–1485.

[2] Q. Fu, E. Saiz, M. N. Rahaman, A. P. Tomsia, Adv. Funct. Mater. 23 (2013) 5461–5476.

[3] S. Bose, G. Fielding, S. Tarafder, A. Bandyopadhyay, Trends Biotech. 31 (2013) 594–605.

[4] M. Bohner, Mater. Today 13 (2010) 24–30.

[5] L. Galea, M. Bohner, J. Thuering, N. Doebelin, C. G. Aneziris, T. Graule, Biomaterials 34 (2013) 6388–6401.

[6] J. M. Hiughes, M. Cameron, K. D. Corwley, Am. Mineral. 74 (1989) 870–876.

[7] K. Kaneda, T. Mizugaki, Energy Environ. Sci. 2 (2009) 655–673.

[8] T. Tsuchida, S. Sakuma, U.S. Patent 8080695 B2, 2011.

[9] J. Xu, T. White, P. Li, C. He, Y.-F. Han, J. Am. Chem. Soc. 132 (2010) 13172–13173.

[10] N. Viswanadham, S. Debnath, P. Sreenivasulu, D. Nandan, S. K. Saxena, A. H. Al-Muhtaseb, RSC Adv. 5 (2015) 67380–67383.

[11] Y. Matsuura, A. Onda, S. Ogo, K. Yanagisawa, Catal. Today 226 (2014) 192–197.

[12] E. G. Rodrigues, T. C. Keller, S. Mitchell, J. Pérez-Ramírez, Green Chem. 16 (2014) 4870–4874.

[13] V. C. Ghantani, S. T. Lomate, M. K. Dongare, S. B. Umbarkar, Green Chem. 15 (2013) 1211–1217.

[14] H. R. Low, M. Avdeev, K. Ramesh, T. J. White, Adv. Mater. 24 (2012) 4175–4179.

[15] S. C. Oh, Y. Wu, D. T. Tran, I. C. Lee, Y. Lei, D. Liu, Fuel 167 (2016) 208–217.

[16] S. Itoh, S. Nakamura, T. Kobayashi, K. Shinomiya, K. Yamashita, S. Itoh, Calcif. Tissue Int. 78 (2006) 133–142.

[17] T. Iwasaki, Y. Tanaka, M. Nakamura, A. Nagai, K. Hashimoto, Y. Toda, K. Katayama, K. Yamashita, J. Am. Ceram. Soc. 91 (2008) 3943–3949.

[18] S. Itoh, S. Nakamura, T. Kobayashi, K. Shinomiya, Biomaterials 27 (2006) 5572–5579.

[19] S. Nakamura, T. Kobayashi, K. Yamashita, Key Eng. Mater. 284–286 (2005) 897–900.

[20] S. Nakamura, T. Kobayashi, M. Nakamura, S. Itoh, K. Yamashita, J. Biomed. Mater. Res. A 92 (2009) 267–275.

[21] M. Nakamura, A. Nagai, T. Hentunen, J. Salonen, Y. Sekilima, T. Okura, K. Hashimoto, Y. Toda, H. Monma, K. Yamashita, ACS Appl. Mater. Interfaces 1 (2009) 2181−2189.

[22] M. Nakamura, N. Hori, S. Namba, T. Toyama, N. Nishimiya, K. Yamashita, Biomed. Mater. 10 (2015) 011001.

[23] C. Fu, K. Savino, P. Gabrys, A. Zeng, B. Guan, D. Olvera, C. Wang, B. Song, H. Ward, Y. Gao, M. Z. Yates, Chem. Mater. 27 (2015) 1164−1171.

[24] M. Rivas, L. J. del Valle, E. Armelin, O. Bertran, P. Turon, J. Puiggalí, C. Alemán, Chem. Phys. Chem. 19 (2018) 1746–1755.

[25] X. Zhang, M. Z. Yates, ACS Appl. Mater. Interfaces 10 (2018) 17232−17239.

[26] M. Rivas, J. Casanovas, L. J. del Valle, O. Bertran, G. Revilla-López, P. Turon, J. Puiggalí, C. Alemán, Dalton Trans. 44 (2015) 9980−9991.

[27] M. Rivas, L. J. del Valle, P. Turon, C. Alemán, J. Puiggalí, Green Chem. 20 (2018) 685−693.

[28] J. Sans, E. Armelin, V. Sanz, J. Puiggalí, P. Turon, J. Catal. 389 (2020) 646−656.

[29] A. Haider, S. Haider, S. S. Han, I. K. Kang, RSC Adv. 7 (2017) 7442–7458.

[30] K. Nakamoto, Infrared and Raman Spectra of Inorganic Coordination Compounds. John Wiley and Sons, New York, 1986.

[31] M. I. Kay, R. A. Young, A. S. Posner, Nature 204 (1964) 1050–1052.

[32] B. Dickens, L. W. Schroeder, W. E. Brown, J. Sol. Stat. Chem. l0 (1974) 232–248.

[33] P. N. de Aza, F. Guitian, C. Santos, S. de Aza, R. Cusco, L. Artis, Chem. Mater. 9 (1997) 916–922.

[34] R. Y. Frost, Y. Xi, R. E. Pogson, G. J. Millar, K. Tan, S. J. Palmer, J. Raman Spectrosc. 43 (2012) 571–576.

[35] G. Penel, G. Leroy, C. Rey, E. Bres, Calcif, Tissue Int. 63 (1998) 475–481.

[36] F. Casciani, R. A. Condrate Sr. Spectrosc. Lett. 12 (1979) 699–713.

[37] R. L. Frost, Y. Xi, R. Scholz, F. M. Belotti, M. Candido, Spectrosc. Lett. 46 (2013) 415–420.

[38] Z. Iqbal, V. P. Tomaselli, O. Fahrenfeld, K. D. MBller, F. A. Ruszala, E. Kostiner, J. Phys. Chem. Solids 38 (1977) 923–927.

[39] L. Moimas, G. de Rosa, V. Sergo, C. Schmid, J. Appl. Biomat. Biomech. 4 (2006) 102–109.

[40] X. Du, Y. Chu, S. Xing, L. Dong, J. Mater. Sci. 44 (2009) 6273–6279.

[41] M. P. Ferraz, F. J. Monteiro, C. M. Manuel, Key Eng. Mater. 240-242 (2003) 555–558.

[42] J. Sans, J, Llorca, V. Sanz, J. Puiggalí, P. Turón, C. Alemán, Langmuir 35 (2019) 14782–14790.

[43] L. Stork, P. Muller, R. Dronskowski, J. R. Ortlepp, Z. Kristallogr. 220 (2005) 201–205.

[44] M. P. Binitha, P. P. Pradyumnan, J. Biomater. Nanobiotechnol. 4 (2013) 119–122.

[45] H. El Boujaady, M. Mourabet, A. El Rhilassi, M. Bennani-Ziatni, R. El Hamrin, A. Taitai, J. Mater. Environ. Sci. 7 (2016) 4049–4063.

[46] A. Dosen, R. F. Giese, Am. Mineral. 96 (2011) 368–373.

[47] A. K. MacMillan, F. V. Lamberti, J. N. Moulton, B. M. Geilich, T. J. Webster, Int. J. Nanomed. 9 (2014) 5627–5637.